Study of the Structural Changes Undergone by Hybrid Nanostructured Si-CNTs Employed as an Anode Material in a Rechargeable Lithium-Ion Battery

ARTICLE *in* THE JOURNAL OF PHYSICAL CHEMISTRY C · JULY 2015

Impact Factor: 4.77 · DOI: 10.1021/acs.jpcc.5b01178

4 AUTHORS:

Javier Palomino

University of Puerto Rico at Rio Piedras

7 PUBLICATIONS **16** CITATIONS

SEE PROFILE

Deepak Varshney

University of Puerto Rico at Rio Piedras

16 PUBLICATIONS **95** CITATIONS

SEE PROFILE

Brad R. Weiner

University of Puerto Rico at Rio Piedras

178 PUBLICATIONS **1,520** CITATIONS

SEE PROFILE

Gerardo Morell

University of Puerto Rico at Rio Piedras

195 PUBLICATIONS **1,324** CITATIONS

SEE PROFILE

THE JOURNAL OF PHYSICAL CHEMISTRY C

Article

pubs.acs.org/JPCC

Study of the Structural Changes Undergone by Hybrid Nanostructured Si-CNTs Employed as an Anode Material in a Rechargeable Lithium-Ion Battery

Javier Palomino,[†,‡] Deepak Varshney,[∥] Brad R. Weiner,[*,†,§] and Gerardo Morell[†,‡]

[†]Institute of Functional Nanomaterials, University of Puerto Rico, San Juan, Puerto Rico 00931, United States

[‡]Department of Physics, University of Puerto Rico, San Juan, Puerto Rico 00936, United States

[§]Department of Chemistry, University of Puerto Rico, San Juan, Puerto Rico 00936, United States

[∥]Advanced Green Innovations, Chandler, Arizona 85226-2401, United States

Supporting Information

ABSTRACT: Silicon−carbon nanotube (Si-CNT) hybrid structures have been fabricated in a single step on Cu substrate by hot filament chemical vapor deposition (HFCVD). A mixture of straight chain saturated aliphatic polymer and Si nanoparticles was used as the seeding source. The material was analyzed by transmission electron microscopy (TEM) and electron energy loss spectroscopy (EELS), and the Si content in the Si-CNT was estimated to be ∼15% wt % by thermogravimetric analysis (TGA). Thereafter, the films were used for lithium-ion battery (LIB) anodes, whose cyclic voltammetry studies show redox peaks for Si and C consistent with lithium insertion/extraction, indicating good reversibility over extensive cycling. Electrochemical tests showed that Si-CNT electrodes can deliver an initial high discharge capacity of ∼700 mAh/g and a reversible capacity of ∼500 mAh/g over 520 cycles. After electrochemical cycling, the Si-CNTs were analyzed and compared to pristine material. The cycled films showed an increment of Si-CNT diameter and negligible cracks, formed due to high volumetric expansion of the silicon upon lithiation. Micro-Raman spectroscopy performed before electrochemical cycling established the presence of crystalline Si nanoparticles (<10 nm), and amorphous Si particles still bound to CNT after cycling. These results were confirmed by X-ray photoelectron spectroscopy (XPS). After cycling, the films showed good contact with the Cu substrate, and delamination was not observed by electrochemical impedance spectroscopy (EIS). The Si-CNT hybrid structure grown in a single step represents a promising anode material for a rechargeable LIB with high energy density and long cycling stability.

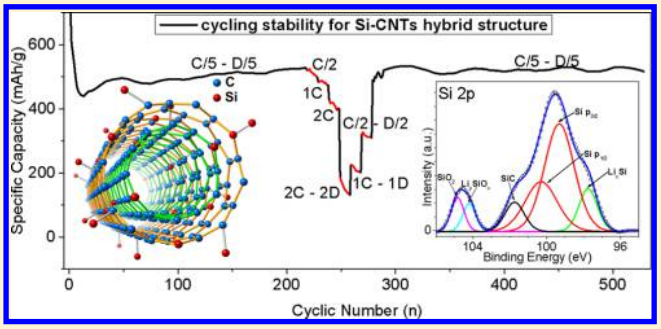

1. INTRODUCTION

During the past decade, numerous researchers around the world have intensely studied lithium-ion batteries (LIBs), because of their high performance in conjunction with electronic devices, electric vehicles, and other applications.[1] The most common material for commercial rechargeable LIB anodes is graphite with high reversibility and stable capacity over hundreds of cycles, but low capacity[2,3] (LiC_6 372 mAh/g) compared to other possible anode materials, such as silicon, which is abundant and nontoxic. It is possible to alloy up to 4 lithium atoms per silicon atom[4] to form a high charge capacity material. The theoretical capacity of the fully lithiated alloy $Li_{4.4}Si$ (4212 mAh/g)[5] is an order of magnitude greater than that of graphite. However, the large silicon volume expansion (>300%)[6,7] upon lithiation leads to high internal stress, electrode pulverization,[8,9] and consequently loss of electrical contact between the active material and current collector, leading to quickly decreasing capacity and poor cycling stability. On the basis of this knowledge, researchers have reported several studies related to battery anodes using silicon nanowires (SiNWs), nanostructured silicon attached to CNT, and Si/C composites, among others.[10−12]

Typically, powder materials such as graphite, graphene flakes, CNTs, and silicon micro/nanostructures are mixed with a polymeric binder forming a composite gel to be spread on copper foil, which is then used as an anode for lithium-ion batteries.[13−16] This method significantly decreases the effective area of the active material exposed to the electrolyte, and degrades the gravimetric and volumetric capacities. In order to avoid polymeric binders, our research group has been studying the direct growth of multiwall carbon nanotubes (MWCNTs) on Cu substrates by HFCVD.[17] This material was used as an anode in LIBs providing a specific capacity greater than graphite,[18] due to Li insertion into large density active sites,

Received: February 4, 2015
Revised: May 16, 2015
Published: July 22, 2015

DOI: 10.1021/acs.jpcc.5b01178
J. Phys. Chem. C 2015, 119, 21125−21134

located on the nanotube surface, inside the nanotubes, and between the MWCNT layers. Additionally, the MWCNT was coated with Si and N by RF sputtering,[19] obtaining a capacity of ~2000 mAh/g for the first discharge at 0.02 mA/cm^2. Furthermore, we implemented the use of straight chain saturated aliphatic polymer as a seeding source for growing graphene,[20] diamond,[21] CNTs,[22] and Si−C nanotube hybrids, because the polymer accelerates the carbon based materials growth, due to its fast decomposition at low temperatures (starting at ~113 °C). Sun et al.[23] used MWCNTs as a template to synthesize diverse silicon−carbon nanostructures by decomposing SiO at 1250 °C in a tube furnace, in which 4 substrates were inserted and exposed to different temperatures. Besides the β-SiC nanowires, multiwalled silicon carbide nanotubes were detected, with interlayer spacing greater than pure CNTs (3.4 Å), consistent with the incorporation of silicon into CNTs by substitution of carbon atoms. Pham-Huu et al.[24] used shape memory synthesis and got comparable silicon−carbon nanotube structures with interlayer spacing of 3.6 Å. Mavrandonakis[25] et al. studied in detail the hybrid structure by theoretical *ab initio* method showing that the Si-CNT structure remains stable as long as the concentration of silicon is less than that of carbon. At higher concentrations, the Si-rich tubes collapse to nanowires due to sp^3 three-dimensional perturbations. Additionally, they observed that increasing the silicon content in CNT expands its diameter, since the Si−C bond length is greater than C−C bond length; consequently, the interlayer spacing increases, confirming the experimental results reported by Sun et al. and Pham-Huu et al.

Taking into account the valuable information related to Si−C nanotubes and the previous works developed by our group, we report, for the first time, the single-step fabrication of Si−C hybrid nanotubes directly on a Cu substrate. The synthesized nanotubes are strongly bound to substrate, and have high surface area and high flexibility to fit volumetric expansion and contraction due to carbon and silicon lithiation. In this hybrid material, CNTs play the roles of mechanical support, ionic and electrical conductor, and lithium storage, while silicon nanoparticles act as local active sites able to deliver high capacity. On the basis of the experimental analysis, we report a new promising anode material for rechargeable LIBs, with high capacity and long cycling stability, as a result of the combined merits of CNTs and silicon.

Compared to other traditional methods to grow hybrid structures that consist of various steps and long deposition times,[11] our method has the advantage of depositing hybrid nanostructures directly on the current collector in a single step and short time (30 min) due to the presence of the saturated aliphatic polymer, which decomposes fast, leaving behind the seeds to grow CNTs. Additionally, the Si source is Si nanoparticles, which are cheap, nontoxic, and nonpyrophoric in contrast to the commonly used silane gas.

2. EXPERIMENTAL SECTION

The Si-CNTs hybrid nanostructure films were grown on Cu substrate, in a custom-made HFCVD chamber, which has been previously described in detail elsewhere.[26,27] We selected rhenium wire as the filament because it is not reactive with carbon and is not consumed during the Si-CNT growing process. Approximately 8 cm of Re wire of 0.5 mm diameter was rolled as a helical spring, and positioned at 8 mm above the substrate. Polycrystalline copper substrates (99.9% pure, 0.5 mm thick, 14 mm disk diameter) were hand polished with different grit sandpaper to remove the oxides and smooth the surface. The substrates were then cleaned in an ultrasonic bath with 2-propanol for 15 min and dried with argon gas. Nickel is a good catalyst to grow carbon nanostructures, because of its significant carbon solubility; thus, Cu substrates were coated with nickel by RF-sputtering. The substrates were fixed to the sputtering holder using carbon tape and placed in the vacuum chamber, which was evacuated to a base pressure of 5×10^{-7} Torr. During the sputtering process, the argon pressure was kept at 20 mTorr, while the target was at a voltage of 1000 V and forward power at ~50 W. The film thickness after 30 min of deposition was ~50 nm. A mixture of 1 g of n-tetracosane (Alpha Aesar), 1 g of n-octacosane (Alpha Aesar), and silicon nanoparticles at the concentration of 20 wt % was melted in a glass beaker on a hot plate at a temperature of 100 °C and heating rate of 10 °C/min with constant stirring for 30 min. A portion of this silicon−polymer melt was transferred onto the nickel coated copper substrate with the help of a glass dropper, forming a thin film with a thickness in the range 0.5−1 μm. The substrate was then inserted in the HFCVD chamber on a molybdenum substrate holder, which is integrated with a graphite heater. Before each deposition, the CVD chamber was evacuated to 5×10^{-7} Torr and then filled with a mixture of 10.0% CH_4 and 90.0% H_2, maintaining the combined flow of gases to 20 sccm, and total pressure at 20 Torr. A constant current of 20 A (~2400 °C) and 4 A (~500 °C) was applied through the rhenium filament and graphite heater, respectively. The deposition time was optimized to 30 min in order to obtain a film that covered the whole substrate. Overall, it is a relatively simple and scalable process that involves single-step deposition of a Si-seeds mixture on the catalytic current collector (Ni−Cu) followed by pyrolysis in the presence of methane.

The initial characterization was done using Raman spectroscopy. The spectra were recorded using a triple monochromator (ISA J-Y model T64000, HORIBA Ltd., Kyoto, Japan), Ar-ion laser excitation (514.5 nm), 80× objective, and the probed area around 1−2 μm^2. The laser power impinging on the sample was kept around 5 mW to avoid sample damage. The silicon substrate was used to calibrate the Raman peak position.

A JEOL JSM-7500F field emission scanning electron microscope (FESEM) was used to analyze surface morphology. The elemental composition of the fabricated material was studied by energy dispersive X-ray spectroscopy (EDS). A Carl Zeiss LEO 922 transmission electron microscope (TEM) operating at 200 kV, including an ω-type energy, electron energy-loss spectroscopy (EELS), was used to analyze the topography and microstructure of the samples. The TEM specimens were prepared from a scratched portion of the film dissolved in ethanol to make a suspension. A drop of the suspension was placed on a copper grid to be analyzed.

The X-ray photoelectron spectroscopy (XPS) experiments were performed at ultrahigh vacuum (UHV) (5.9×10^{-9} Torr) in the Physical Electronic 5600 X-ray photoelectron spectrometer with Al Kα source and 200 mm diameter analyzer. The C 1s, O 1s, and Si 2p high resolution spectra were obtained for Si-CNTs and fitted using PHI-Multipack v9.4 and Casa XPS v2.3 software. The fitting of all spectra was done with mixed Gaussian−Lorentzian line shape, and background was computed by Shirley algorithm.

The silicon content in the Si-CNTs hybrid material was estimated by thermogravimetric analysis (TGA) performed on a PerkinElmer STA6000 instrument, controlled by Pyris

DOI: 10.1021/acs.jpcc.5b01178
J. Phys. Chem. C 2015, 119, 21125−21134

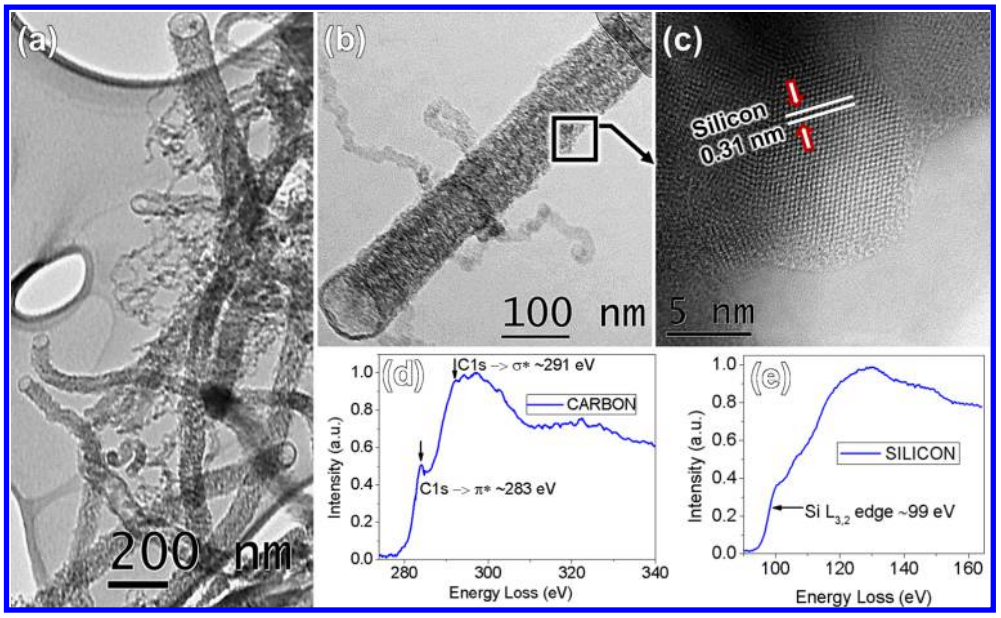

Figure 1. TEM images of (a) Si coated CNT at low magnification, (b) open edge showing the tube cavity, and (c) Si coating at high magnification. EELS spectra obtained on the Si-CNT for (d) carbon and (e) silicon.

software v11, and measured between room temperature and 900 °C, at heating rate of 20 °C/min in air flow.

The mass of the total active material (CNTs + Si) was determined to be 2.4 mg by measuring the mass of the substrate before and after the Si-CNT growth and averaging over five different samples. Coin cells were prepared in an argon atmosphere inside the glovebox (M. Braun). The Si-CNTs hybrid thin film, deposited by a single step in the HFCVD, was used as the working electrode material, while Li-metal foil was employed as a counter and reference electrode. Celgard 2400 membrane was used as an electrode separator. The electrolyte consisted of lithium hexafluorophosphate ($LiPF_6$), dissolved in a mixture of ethylene carbonate (EC) and dimethyl carbonate (DMC) at proportion of 1:1 in volume. A Gamry Instruments potentiostat, PHE200, EIS300, and electrochemical software were used to perform cyclic voltammetry (CV), charge−discharge, and electrochemical impedance spectroscopy (EIS) measurements. Following cycling, the coin cells were disassembled in an argon atmosphere (glovebox) for additional characterization. In order to remove residual carbonate solvents and $LiPF_6$ salt, the electrodes were soaked in 2 mL of dimethyl carbonate (DMC) for 30 min, and then gently rinsed with DMC and dried for 1 h at ambient temperature.

3. RESULTS AND DISCUSSION

The TEM images in Figure 1a,b show that the Si-CNTs hybrid nanostructures consist of multiwall carbon nanotubes with diameters around ∼100 nm and are uniformly coated with silicon nanoparticles. The planes of CNTs are blurred due to the Si coating on them. However, the inner cavity of the Si-CNTs structure is clearly seen through the open edge (Figure 1b). Figure 1c shows the lattice fringes of the Si coating, revealing an interplanar spacing of about 0.31 nm, which matches with the (111) orientation of Si, consistent with previous report.[28] The carbon EELS spectra (Figure 2c,d) show the energy loss peaks of the 1s → π^* (∼283 eV) and 1s → σ^* bonds (∼291 eV). The C K-edge shifted to lower energies (from pure carbon at 284 to 283.1 eV), consistent with Si−C

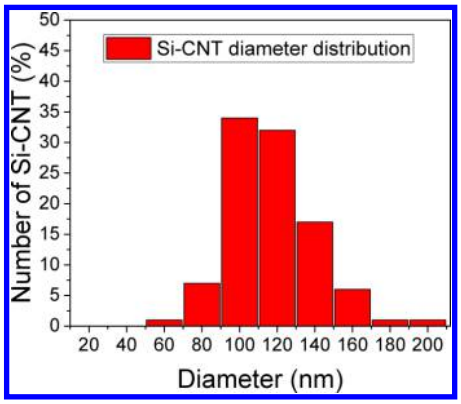

Figure 2. Distribution histogram of nanotube diameters deduced from representative TEM images.

hybrid structures,[29,30] whereas the Si $L_{3,2}$ edge shifts to higher energies (from pure silicon's 100 eV value to 100.5 eV), implying a strong Si−C chemical bonding due to the higher electronegativity of carbon compared to that of silicon. In general, the carbon EELS spectral profiles of Si-CNTs match well with those of pure CNTs, while the silicon EELS spectral profiles correspond to pure Si and some SiO_x (shoulder at ∼105 eV) due to contamination.[29,31]

A representative diameter distribution of Si-CNT is depicted in Figure 2. The histogram shows that the nanotube diameters range from 70 to 170 nm.

In order to determine the amount of silicon present in the Si-CNT material, we performed TGA measurements (Figure 3), where the initial mass of Si-CNT material (6.2 mg) was achieved from various samples by scratching carefully from the copper substrate. The TGA profiles (weight loss and weight loss derivative) show the first weight loss event at around 400 °C, due to the sublimation of amorphous carbon, other noncrystalline carbon materials, and environmental contaminants.[32] As the temperature is increased, significant weight loss starts taking place at ∼580 °C with a maximum at ∼685 °C, and continuing until ∼750 °C, which is due to the oxidation of

DOI: 10.1021/acs.jpcc.5b01178
J. Phys. Chem. C 2015, 119, 21125−21134

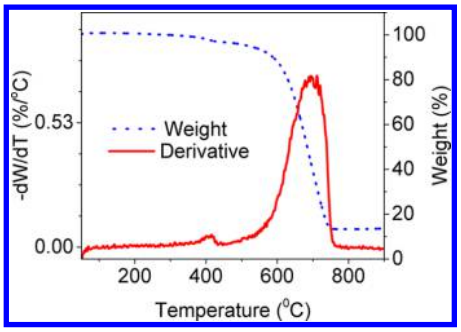

Figure 3. TGA measurements and the corresponding derivative curve for Si-CNTs material.

CNTs into CO_2.[33] After the sublimation of C was completed, 14.5 ± 0.3 wt % of the material remained, which corresponds to Si. This result was also confirmed by inductive coupled plasma-optical emission spectrometry (ICP-OES) not shown.

From the characterization results described above, we propose a qualitative schematic representation (Figure 4) of the Si-CNT hybrid structures consisting of multiwall CNTs with most of the Si atoms coating the nanotube surface and some Si atoms inserted in the nanotube walls.

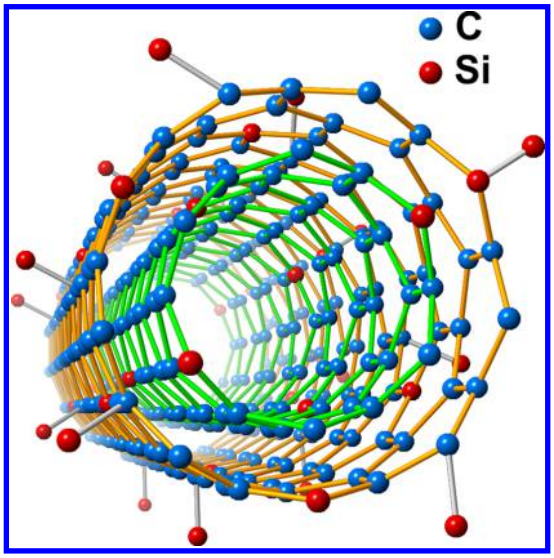

Figure 4. Schematic representation of a Si-CNT.

We propose the following qualitative growth mechanism to understand the formation of the Si-CNTs hybrid structures in the HFCVD environment. The polymer employed consists of a long straight chain of *n*-alkanes ($CH_3[CH_2]_nCH_3$) with melting point of ∼50 °C and flash point starting at ∼113 °C (Figure 5i). At the substrate temperature of ∼500 °C, the polymer decomposes into hydrocarbon radicals (CH_x) leaving behind sp^2 fragments[34] on the Cu substrate surface which act as nucleation centers for CNT growth, hydrogen escapes, and carbon gets dissolved into the Ni catalyst. Meanwhile, atomic hydrogen attacks the oxide layer of the Si nanoparticles,[35] leaving the bare Si exposed to the chemical vapor and in contact with the Ni catalyst. Consequently, both carbon and silicon atoms are dissolved into the Ni catalyst, with Si as the minor component (as depicted in Figure 5ii). These processes produce the conditions for the growth of Si-CNTs hybrid structures following the standard base-growth model mechanism under a CH_4 atmosphere (Figure 5iii).[36−38]

The above-described Si-CNTs hybrid nanostructures were used for LIB anodes, whose electrochemical properties were studied by cyclic voltammetry, charge−discharge measurements, and electrochemical impedance spectroscopy. The cathodic region of the voltammogram (Figure 6a) shows a peak at around 0.01, corresponding to the formation of LiC_6,[19] a peak at around 0.21 V attributed to the formation of Li_xSi,[39−42] a peak at around 0.30 V ascribed to the irreversible reaction of Li ions with hydroxyl and other functional groups[39] coming from ambient contamination, and two peaks at around 1.8 and 1.25 V corresponding to the formation of the solid electrolyte interface (SEI).[18,19,43] The anodic smooth band in the 0.15−0.35 V range corresponds to the extraction of Li from LiC_6 sites,[44] whereas the oxidation peak at around 490 mV is attributed to the extraction of Li from Li_xSi sites.[41,45] From the second to the fifth cycle, the voltammograms remain essentially constant, indicating good reversibility of Li reactions and structural stability of Si-CNT hybrid nanostructures.

The specific capacity profiles of Si-CNT hybrid material, performed on coin cells at a constant current density of 100 mA/g between 0.01 and 3.0 V, are shown in Figure 6b. The charge−discharge curves suggest that this hybrid nanostructure retains the active electrochemical performance of reversible lithium alloying and dealloying even after 520 cycles. The first discharge cycle is characterized by high discharge capacity ∼707 mAh/g and plateaus at voltages around 1.8, 1.25, and 0.3. Such plateaus are typical of carbon based anodes, and are related to the decomposition of the electrolyte and the generation of a passivated film or the formation of the SEI.[13,46] The plateaus were not observed from the second cycle onward, indicating that SEI formation was complete in the first cycle itself. These results are consistent with the previously discussed cyclic voltammetry results (Figure 6a). Considering the active material (2.4 mg) on the substrate of radius 0.7 cm, the current density was calculated to be 0.16 mA/cm^2 and the areal capacity calculated is shown in Figure SI-2.

Details of the experiments conducted to study the cycling stability of Si-CNTs anodes over 520 cycles are shown in Figure 6c. After an initial discharge capacity of 707 mAh/g, the Si-CNTs nanostructures achieved capacity retention of 69%, 71%, and 75% at the end of 50, 100, and 200 cycles, respectively. Small increases in discharge capacity were observed from the 21st cycle forward, possibly due to the stimulation of more silicon atoms dynamically reacting with lithium ions.[11] The Si-CNT based anode achieved a reversible specific capacity of 510 mAh/g, which is higher than the theoretical (372 mAh/g) and experimental (∼275 mAh/g) capacity reported for graphite over the voltage range 0.01−2.5 V versus Li/Li+.[47]

The systematic variation of the charge (C) and discharge (D) current densities showed that the capacity retention is strongly dependent on the C and D rates. The 1C rate based on the reversible capacity at low rate is 500 mA/g. Keeping constant the D-rate and varying the C-rate yielded high reversible capacities for C/5, C/2.5, 1C, and 2C, of 526, 507, 484, and 404 mAh/g, respectively. Further, when the C and D rates were changed to 2C, 1C, C/2.5, and C/5, the capacities were 150, 216, 314, and 514 mAh/g, respectively. Therefore, the original stable capacity was fully recovered, indicating good reversibility, robustness, and stability of the anode hybrid material.

DOI: 10.1021/acs.jpcc.5b01178
J. Phys. Chem. C 2015, 119, 21125−21134

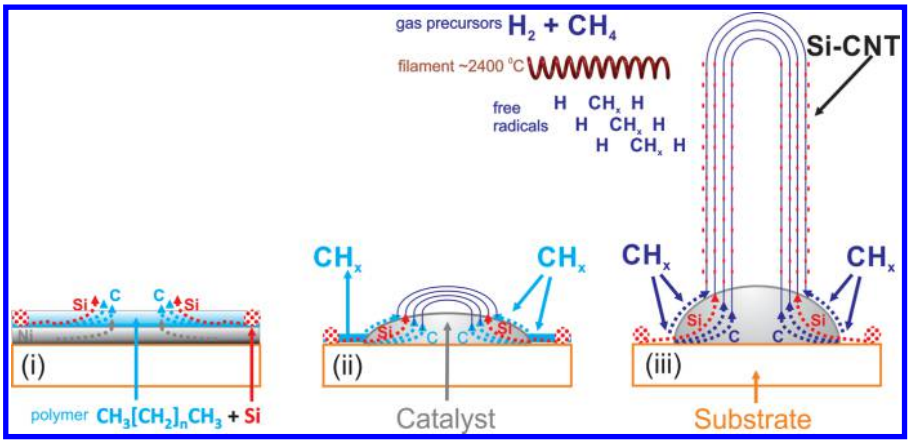

Figure 5. Base-growth mechanism for Si-CNT: As the substrate temperature is incremented, (i) the aliphatic polymer decomposes to produce hydrocarbon radicals mixed with Si atoms, (ii) Ni nanoislands aggregate to catalyze the formation of nucleation centers, and (iii) the Si-CNT growth continues from the base with added H_2 and CH_4.

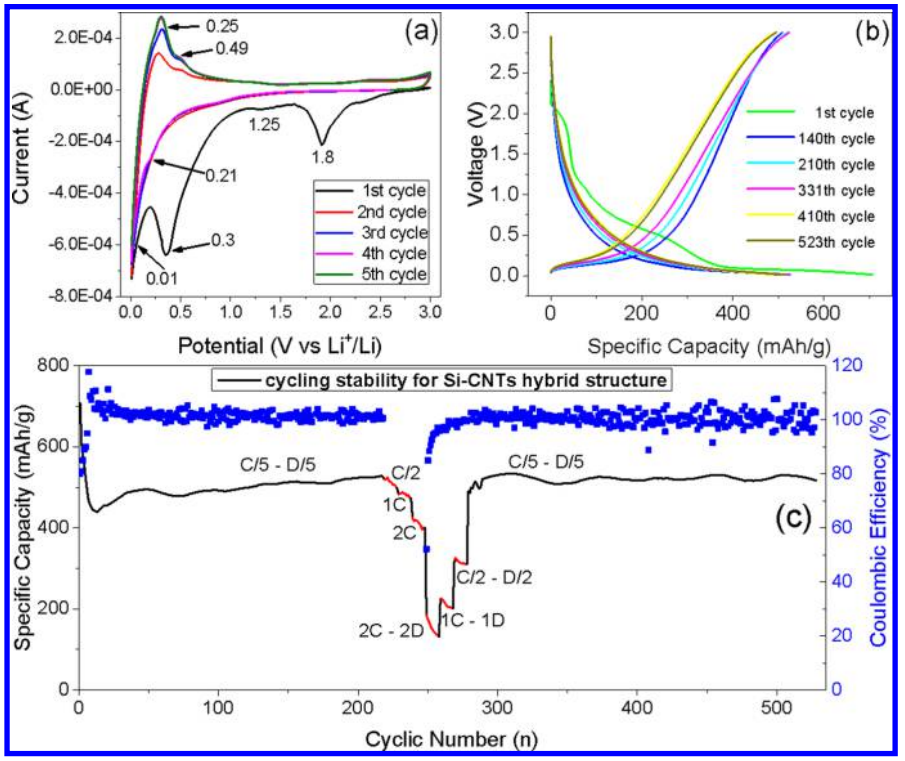

Figure 6. (a) Cyclic voltammograms of Si-CNTs hybrid material. (b) Charge−discharge (C−D) profiles of Si-CNT hybrid material anodes. (c) Cyclic performance and its columbic efficiency of the Si-CNT anode at different current rates.

Table 1. Summary of the Electrochemical Data Compared with Results from the Literature

active material	first discharge capacity (mAh/g)	reversible capacity (mAh/g)	capacity fading %	no. cycles	Coulombic efficiency (%)
SiOC−CNT[52]	842	686	19	40	~99
Si−Al−C−N/CNT[51]	577	400	30	1100	NA
Si(B)CN-CNT[53]	768	412	47	30	NA
Si-CNT Si: 75 wt %[11]	2552	1000	60	100	~99
SiN-CNT[19a]	2000	307	85	10	NA
Si-CNT Si: 15 wt %[b]	707	500	30	520	~99

[a]Previous work. [b]Present work.

The reversible capacity of our anode materials could potentially be improved by increasing the Si content. As we moved from 10 wt % to 15 wt %, we observed an increase in the reversible capacity from ~450 mAh/g over 70 cycles (data available in Supporting Information; see Figure SI-1) to a value of ~500 mAh/g over 520 cycles, respectively. However, at concentrations of 20 wt % and higher, the half cell presents a rapid capacity fading due to anode degradation, ascribed to

DOI: 10.1021/acs.jpcc.5b01178
J. Phys. Chem. C 2015, 119, 21125−21134

collapse of the tubular structure due to three-dimensional perturbations.[23,24]

Figure 6c shows that the Coulombic efficiency is initially low, which can be ascribed to the formation of SEI. The first cycle loss can be mitigated by coating the active material with artificial SEI films[48] like N-UNCD,[49] or by pre-lithiation of the anode material.[50] For cycles in the range 220−280, the efficiency varies as a direct consequence of the variation of charge and discharge current rates used to observe these effects. In general, the efficiency was calculated to be ∼99%, which means high reversibility over 520 cycles.

Several Si/CNT based materials have been studied for battery applications, as shown in Table 1. Previously, we reported CNT coated with Si−N by sputtering,[19] which showed a high initial discharge capacity (2000 mAh/g) but poor reversibility. This problem is addressed by using the present Si-CNT hybrid material. The first discharge capacity of Si-CNT (707 mAh/g) is comparable to the published values, except for the results reported by Wang et al.[11] who incorporated Si ∼ 75 wt %, but the fabrication process required many steps, the use of pyrophoric silane, and the transfer of the material from the quartz substrate to the current collector. The present Si-CNT material shows better reversibility compared to published values, except for the results of David et al.[52] who reported a capacity fading of only 30% after 1100 cycles, but a low reversible capacity (400 mAh/g) compared to our results.

In order to ascertain the suitability of the Si-CNT material as battery anode, we compare its properties with those of the anode material of a commercial coin cell lithium battery (CLB2032) with a nominal capacity of 50 mAh as specified by the manufacturer (see Table 2). The commercial coin cell

Table 2. Si-CNT Hybrid Material Compared to Commercial Rechargeable Coin Cell Material

property	commercial CLB2032	Si-CNT coin cell
material loading (mg/cm^2)	12	1.6
specific capacity (mAh/g)	140	510
specific current density (mA/g)	27.8	100
areal capacity at 12 mg/cm^2 (mAh/cm^2)	1.7	5.9

anode has a high material loading of ∼12 mg/cm^2 compared to ∼1.56 mg/cm^2 for Si-CNT. However, the material loading of the Si-CNT can be enlarged by growing thicker films, compressing them,[54] and using the jelly roll anode design. The specific capacity of Si-CNT is about 3 times greater than that of the commercial battery, indicating that Si-CNT is a promising material for rechargeable batteries required for modern devices and space applications. The areal capacity normalized for a material loading of 12 mg/cm^2 is also about 3 times larger for Si-CNT than that for the commercial material.

Figure 7 shows the FESEM images of Si-CNTs hybrid structures before and after electrochemical cycling. Figure 7a,b reveal, at different magnifications, the high density of interconnected tube-shaped nanostructures with diameters in the 50−100 nm range and lengths in the 10−20 μm range. A representative line-scan EDS spectrum (Figure 7c) taken radially across a Si-CNT shows the following: C is the main component in the nanostructure as expected, Si is the second largest component and homogeneously distributed, and a negligible amount of oxygen attributed to SiO_x, consistent with atmospheric contamination.

Figure 7d shows the surface morphology of the anode material after 520 charge−discharge cycles. It can be seen that the Si-CNT diameter increased from ∼100 to ∼150 nm due to the formation of a robust and stable SEI. No visible cracks were found on the anode material after extensive Li alloying/dealloying, the anode retained its good contact with the current collector, and no anode paring was observed. These structural observations are consistent with the excellent capacity retention shown in Figure 6c.

The Raman spectra in Figure 8a,b correspond to the Si-CNT anodes before and after 520 charge−discharge cycles, respectively. The pristine anodes show spectral features around 195, 506, 750, 970, 1351, 1580 cm^{-1}. The 1580 cm^{-1} (G-band) band is associated with the crystalline graphite-like materials.[55,56] The band at 1351 cm^{-1} (D-band) arises due to defects in the crystalline graphite-like materials.[57] The intensity of the D-band is higher than that of the G-band, consistent with the significant amount of mass disorder caused by the insertion of Si atoms into CNTs.[58] The band around 195 cm^{-1} corresponds to the radial breathing mode (RBM) of Si-CNT hollow structures with very reduced diameter (∼1.2 nm).[56] The broad band around 750 cm^{-1} is attributed to nanocrystalline SiC.[59] The peaks at around 506 and 970 cm^{-1} are the first-order and second-order, respectively, transverse optical (TO) phonon modes of Si nanoparticles of about 8 nm.[60,61]

After 520 charge−discharge cycles, the Raman spectrum (Figure 8b) shows broadening of the Si TO mode, indicating amorphization of the Si nanoparticles upon lithiation/delithiation processes.[8,9,62] The rest of the Raman features remain essentially unchanged after extensive cycling, consistent with the robustness and excellent capacity retention shown in Figure 6c.

High resolution XPS was used to determine the chemical state and elemental composition of Si-CNTs hybrid material before (Figure 9a−c) and after electrochemical cycling (Figure 9d−f). For the pristine anode material, the chemical states of Si represented by the asymmetrical and broad band Si 2p (Figure 9a) were deconvoluted into six peaks. The first two peaks at ∼99.5 and ∼100.2 eV correspond to Si^0 2p$_{3/2}$ and Si^0 2p$_{1/2}$. The third peak at ∼100.7 eV is associated with SiC.[63] Additionally, silicon suboxides are represented by three peaks at ∼102.2 eV (SiO), ∼103.7 eV (Si_2O_3), and ∼104.7 eV (SiO_2),[64,65] due to ambient contamination.

The C 1s band can be represented by the superposition of five peaks (Figure 9b). The first peak at ∼283.4 eV is associated with silicon carbide,[63,66] consistent with the Si 2p peak at ∼100.7 eV, while the second peak that dominates the region centered at ∼284.5 eV is assigned to graphitic carbon. The third peak centered at ∼286.3 eV is attributed to SiCO,[66] and the next two peaks are related to C═O and COOH,[66−70] consistent with atmospheric contamination of the Si-CNTs.[70]

The presence of C−O and Si−O bonds is also evident in the O 1s spectra recorded before electrochemical cycling. The O 1s band can be resolved into three peaks (Figure 9c). The first two peaks at ∼530.3 and ∼531.5 eV are associated with carbonates (CO_x, COOH) and the peak centered at ∼532.6 is attributed to silicon oxides.[64,65] The XPS analysis is consistent with the formation of the Si-CNTs hybrid material with some contamination due to air exposure.

The XPS spectra of the anode material after 520 charge−discharge cycles are shown in Figure 9d−f. The Si 2p, C 1s, and O 1s regions show the presence of Li bonds. In the Si 2p spectrum, the peaks at ∼98 and ∼104 eV are attributed to Li_xSi

DOI: 10.1021/acs.jpcc.5b01178
J. Phys. Chem. C 2015, 119, 21125−21134

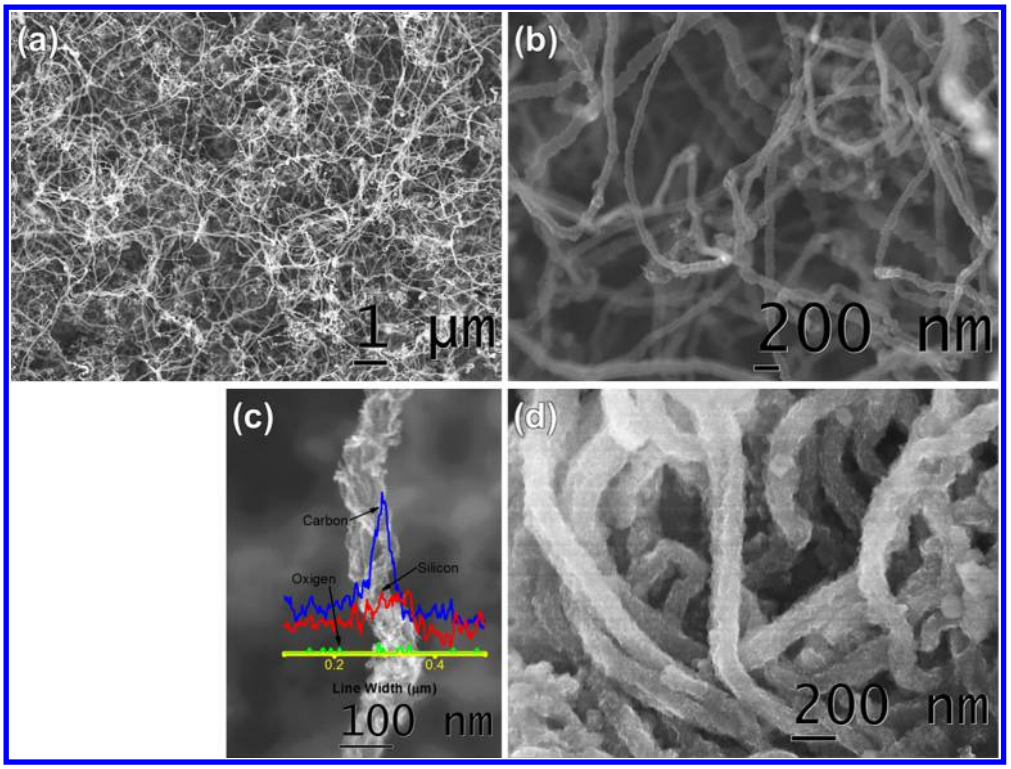

Figure 7. FESEM images of Si-CNTs: (a) high density tubular structures with large aspect ratio and (b) Si coated CNTs with diameter less than 100 nm. (c) EDS line-scan across of Si-CNT showing the elemental composition, and (d) FESEM images of Si-CNTs hybrid material electrode after 520 charge−discharge cycles.

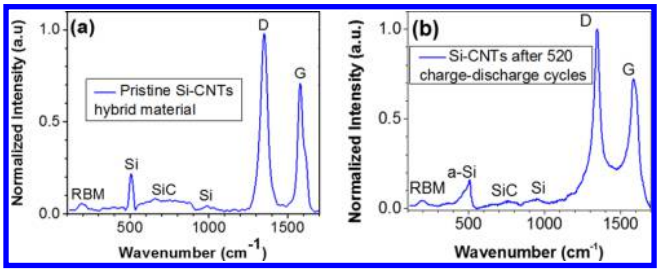

Figure 8. Raman spectra of (a) pristine Si-CNTs hybrid material and (b) after 520 charge−discharge cycles.

and of Li_ySiO_x, respectively.[71] In the C 1s spectrum, a new CO_3 phase is revealed at ∼290 eV, which can be attributed to Li_2CO_3 and lithium alkyl carbonates, which were reported as SEI components in graphite electrodes.[71] In the O 1s spectra, the peak at ∼531 eV is assigned to Li_2CO_x.[72] The XPS data of the cycled anode material show the formation of Li−Si and Li−C bonds as expected for a Si-CNTs hybrid material. All of the XPS peaks of the pristine material are also present in the cycled material, suggesting its integrity during cycling, and consistent with the stability of the charge−discharge capacity.

In order to understand the relationship between the Si-CNT nanostructure with the electrochemical properties before and after applying different charge and discharge currents rates over extensive cycling (Figure 6c), electrochemical impedance spectroscopy (EIS) was carried out at 100 and 500 cycles of galvanostatic charge and discharge. The Nyquist plot (Figure 10) consists of an oblique straight line at low frequencies, attributed to lithium-ion diffusion in the bulk of the anode material consistent with the typical Warburg impedance, and a suppressed semicircle at the middle-high frequencies, attributed to charge-transfer processes. The suppressed semicircle is consistent with the overlap of two semicircles, one semicircle in the high frequency region corresponding to the surface layer resistance (R_{sl}) due to the SEI formation, and the middle frequency semicircle corresponding to the charge transfer resistance (R_{ct}) across the interface. The intercept value on the horizontal-axis (∼15.7 Ω) in the high frequency region corresponds to the solution resistance (R_{sol}) due to the lithium-ion conduction in the electrolyte.

The Nyquist plots demonstrate that the spectrum at the 100th cycle is almost the same that at the 500th cycle, meaning there is a good electrical contact between the active materials and the current collector, as well as good structural stability of the Si-CNTs hybrid material, even after varying the charge−discharge current rate in a wide range, as shown by the cycling stability plot (Figure 6c). This information was confirmed by simulating the Nyquist plot data in terms of the impedance, where we resolved the equivalent circuit (inset of Figure 10) integrated by Warburg impedance Z_w; constant phase elements C_{dl}, C_{sl}; and the resistances R_{sol}, R_{sl}, R_{ct} described above.

Table 3 shows that the values of R_{sol}, R_{ct}, and R_{sl} increased slightly from the 100th to the 500th cycle, which is consistent with the robustness and high stability of Si-CNTs hybrid structure upon the lithiation/delithiation over more than 500 cycles, and even applying different high charge−discharge current rates. These results are in good agreement with the cycling stability, SEM images, and Raman spectrum after cycling, observed in Figures 6c, 7d, and 8b, respectively.

On the basis of the mechanism of growing Si-CNT hybrid material, the structure model presented, all of the characterizations, and the electrochemical measurements, we determined that the implementation of high capacity silicon atoms bonded to carbon nanotubes is the main factor contributing to improvement of the electrochemical performance of the

DOI: 10.1021/acs.jpcc.5b01178
J. Phys. Chem. C 2015, 119, 21125−21134

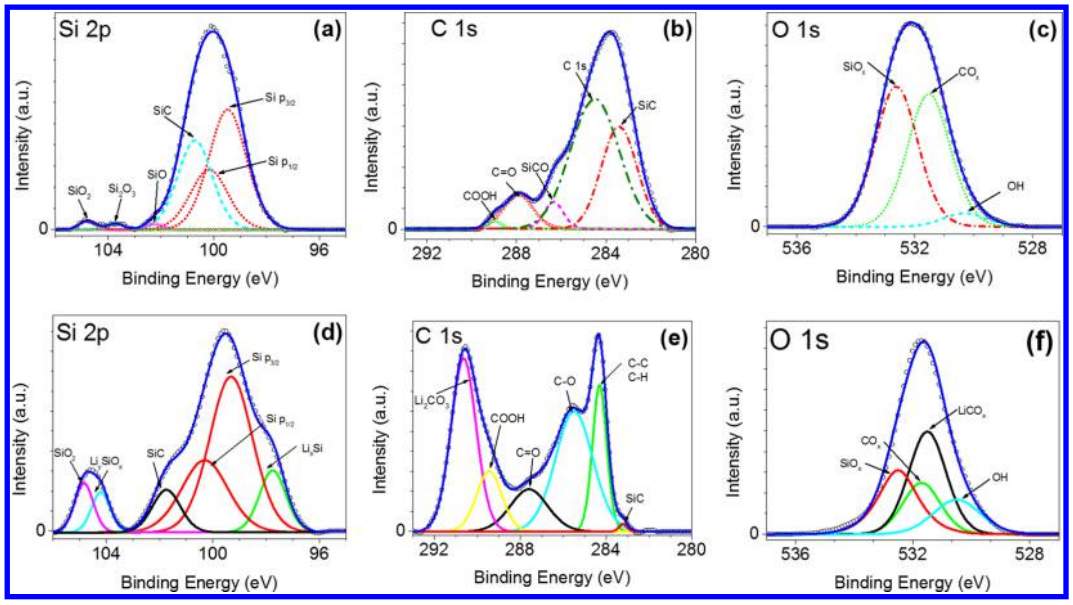

Figure 9. XPS spectra of pristine Si-CNTs corresponding to (a) Si 2p, (b) C 1s, and (c) O 1s. XPS spectra of Si-CNTs after 520 cycles corresponding to (d) Si 2p, (e) C 1s, and (f) O 1s.

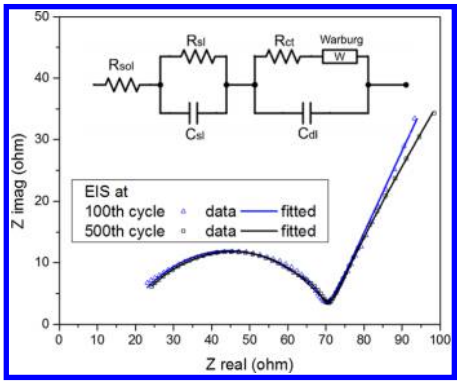

Figure 10. Impedance spectra of Si-CNTs hybrid material anodes at 100th and 500th cycles in charged state. Inset represents the equivalent circuit used to fit the spectra.

Table 3. EIS Data Parameters Obtained after Fitting from the Model Shown in the Inset of Figure 10

fitted parameter	100th cycle	500th cycle
R_{sol} (Ω)	14.6	16.8
R_{ct} (Ω)	59.3	68.1
R_{sl} (Ω)	16.3	25.6

lithium-ion coin cells. Moreover, the core Si-CNTs enhance the transportation of both electrons and lithium ions to and from the neighboring silicon nanoclusters, which act as the lithium alloying and dealloying local sites.

4. CONCLUSIONS

A novel Si-CNT hybrid material has been successfully fabricated in a single step on Cu substrate by HFCVD for lithium-ion battery anodes. A mixture of polymer and Si nanoparticles used as the seeding source is the key to growing the Si-CNTs hybrid structure which consists of Si coated multiwall silicon−carbon nanotubes of diameters in the range 80−100 nm, as demonstrated by TEM images and EELS analysis. The Si content in the Si-CNT hybrid material was estimated by TGA, and it was found to be ∼15 wt %. Electrochemical tests showed that the Si-CNT anode is able to deliver an initial high discharge capacity of around 700 mAh/g and a reversible capacity of ∼500 mAh/g over 520 cycles. The CV studies showed redox peaks for CNT and Si corresponding to lithium insertion/extraction, and indicated good reversibility over extensive cycling, which was verified by cycling stability measurements. The analysis before and after electrochemical cycling performed by micro-Raman spectroscopy established that the Si-CNT structure is highly stable, which was confirmed by EIS. FESEM showed the formation of a robust and stable SEI with no visible cracks on the anode material; XPS demonstrated the formation of Li−Si and Li−C bonds, as expected. All the analyses suggested the integrity of Si-CNT over extensive cycling. We conclude that Si-CNTs represent a promising anode material for rechargeable lithium-ion batteries with high energy density, and long cycling stability.

■ ASSOCIATED CONTENT

Supporting Information

The Supporting Information is available free of charge on the ACS Publications website at DOI: 10.1021/acs.jpcc.5b01178.

Charge−discharge profile and areal capacity data (PDF)

■ AUTHOR INFORMATION

Corresponding Author

*E-mail: brad@hpcf.upr.edu.

Author Contributions

The manuscript was written through contributions of all authors. All authors have given approval to the final version of the manuscript.

Notes

The authors declare no competing financial interest.

■ ACKNOWLEDGMENTS

This research was made possible by funds from PR DOE EPSCoR (DOE Grant DEFG02-08ER46526, J.P.) and PR NASA EPSCoR (NASA Cooperative Agreement NNX15A-K43A). We would like to acknowledge the IFN Nanoscopy

DOI: 10.1021/acs.jpcc.5b01178
J. Phys. Chem. C 2015, 119, 21125−21134

Facility (NSF Cooperative Agreement EPS-01002410) at UPR-RP for permitting us to use the electron microscopes. We also acknowledge the Speclab Facilities for access to the Raman Spectrometer, and the Material Characterization Center in the Molecular Sciences Research Building for the TGA and XPS measurements. Special thanks to Rebeca Rivera for proof-reading this manuscript.

REFERENCES

(1) Etacheri, V.; Marom, R.; Elazari, R.; Salitra, G.; Aurbach, D. Challenges in the Development of Advanced Li-Ion Batteries: A Review. *Energy Environ. Sci.* **2011**, *4*, 3243−3262.
(2) Satoh, A. Electrochemical Intercalation of Lithium into Graphitized Carbons. *Solid State Ionics* **1995**, *80*, 291−298.
(3) Landi, B. J.; Ganter, M. J.; Cress, C. D.; DiLeo, R. A.; Raffaelle, R. P. Carbon Nanotubes for Lithium Ion Batteries. *Energy Environ. Sci.* **2009**, *2*, 638−654.
(4) Boukamp, B. A. All-Solid Lithium Electrodes with Mixed-Conductor Matrix. *J. Electrochem. Soc.* **1981**, *128*, 725−729.
(5) Szczech, J. R.; Jin, S. Nanostructured Silicon for High Capacity Lithium Battery Anodes. *Energy Environ. Sci.* **2011**, *4*, 56−72.
(6) Liu, X. H.; Zhang, L. Q.; Zhong, L.; Liu, Y.; Zheng, H.; Wang, J. W.; Cho, J.-H.; Dayeh, S. A.; Picraux, S. T.; Sullivan, J. P.; et al. Ultrafast Electrochemical Lithiation of Individual Si Nanowire Anodes. *Nano Lett.* **2011**, *11*, 2251−2258.
(7) Liu, X. H.; Zheng, H.; Zhong, L.; Huang, S.; Karki, K.; Zhang, L. Q.; Liu, Y.; Kushima, A.; Liang, W. T.; Wang, J. W.; et al. Anisotropic Swelling and Fracture of Silicon Nanowires during Lithiation. *Nano Lett.* **2011**, *11*, 3312−3318.
(8) Liu, X. H.; Zhong, L.; Huang, S.; Mao, S. X.; Zhu, T.; Huang, J. Y. Size-Dependent Fracture of Silicon Nanoparticles during Lithiation. *ACS Nano* **2012**, *6*, 1522−1531.
(9) Gu, M.; Li, Y.; Li, X.; Hu, S.; Zhang, X.; Xu, W.; Thevuthasan, S.; Baer, D. R.; Zhang, J.-G.; Liu, J.; Wang, C. In Situ TEM Study of Lithiation Behavior of Silicon Nanoparticles Attached to and Embedded in a Carbon Matrix. *ACS Nano* **2012**, *6*, 8439−8447.
(10) Terranova, M. L.; Orlanducci, S.; Tamburri, E.; Guglielmotti, V.; Rossi, M. Si/C Hybrid Nanostructures for Li-Ion Anodes: An Overview. *J. Power Sources* **2014**, *246*, 167−177.
(11) Wang, W.; Kumta, P. N. Nanostructured Hybrid Silicon/carbon Nanotube Heterostructures: Reversible High-Capacity Lithium-Ion Anodes. *ACS Nano* **2010**, *4*, 2233−2241.
(12) Kasavajjula, U.; Wang, C.; Appleby, A. J. Nano- and Bulk-Silicon-Based Insertion Anodes for Lithium-Ion Secondary Cells. *J. Power Sources* **2007**, *163*, 1003−1039.
(13) Varzi, A.; Täubert, C.; Wohlfahrt-Mehrens, M.; Kreis, M.; Schütz, W. Study of Multi-Walled Carbon Nanotubes for Lithium-Ion Battery Electrodes. *J. Power Sources* **2011**, *196*, 3303−3309.
(14) Yang, S.; Song, H.; Chen, X.; Okotrub, A. V.; Bulusheva, L. G. Electrochemical Performance of Arc-Produced Carbon Nanotubes as Anode Material for Lithium-Ion Batteries. *Electrochim. Acta* **2007**, *52*, 5286−5293.
(15) Park, M.-H.; Kim, M. G.; Joo, J.; Kim, K.; Kim, J.; Ahn, S.; Cui, Y.; Cho, J. Silicon Nanotube Battery Anodes. *Nano Lett.* **2009**, *9*, 3844−3847.
(16) Obrovac, M. N.; Christensen, L. Structural Changes in Silicon Anodes during Lithium Insertion/Extraction. *Electrochem. Solid-State Lett.* **2004**, *7*, A93−A96.
(17) Katar, S. L.; González-Berríos, A.; De Jesus, J.; Weiner, B.; Morell, G. Direct Deposition of Bamboo-Like Carbon Nanotubes on Copper Substrates by Sulfur-Assisted HFCVD. *J. Nanomater.* **2008**, *2008*, 1−7.
(18) Katar, S. L.; De Jesus, J.; Weiner, B. R.; Morell, G. Films of Bamboo-like Carbon Nanotubes as Electrode Material for Rechargeable Lithium Batteries. *J. Electrochem. Soc.* **2008**, *155*, A125−A128.
(19) Katar, S. L.; Hernandez, D.; Biaggi Labiosa, A.; Mosquera-Vargas, E.; Fonseca, L.; Weiner, B.; Morell, G. SiN/Bamboo like Carbon Nanotube Composite Electrodes for Lithium Ion Rechargeable Batteries. *Electrochim. Acta* **2010**, *55*, 2269−2274.
(20) Varshney, D.; Venkateswara Rao, C.; Guinel, M. J.-F.; Ishikawa, Y.; Weiner, B. R.; Morell, G. Free Standing Graphene-Diamond Hybrid Films and Their Electron Emission Properties. *J. Appl. Phys.* **2011**, *110*, 044324−1−044324−6.
(21) Varshney, D.; Kumar, A.; Guinel, M. J.-F.; Weiner, B. R.; Morell, G. Spontaneously Detaching Self-Standing Diamond Films. *Diamond Relat. Mater.* **2012**, *21*, 99−102.
(22) Varshney, D.; Sumant, A. V.; Weiner, B. R.; Morell, G. Growth of Carbon Nanotubes on Spontaneously Detached Free Standing Diamond Films and Their Field Emission Properties. *Diamond Relat. Mater.* **2012**, *30*, 42−47.
(23) Sun, X.-H.; Li, C.-P.; Wong, W.-K.; Wong, N.-B.; Lee, C.-S.; Lee, S.-T.; Teo, B.-K. Formation of Silicon Carbide Nanotubes and Nanowires via Reaction of Silicon (from Disproportionation of Silicon Monoxide) with Carbon Nanotubes. *J. Am. Chem. Soc.* **2002**, *124*, 14464−14471.
(24) Pham-Huu, C.; Keller, N.; Ehret, G.; Ledoux, M. J. The First Preparation of Silicon Carbide Nanotubes by Shape Memory Synthesis and Their Catalytic Potential. *J. Catal.* **2001**, *200*, 400−410.
(25) Mavrandonakis, A.; Froudakis, G. E.; Schnell, M.; Mühlhäuser, M. From Pure Carbon to Silicon−Carbon Nanotubes: An Ab-Initio Study. *Nano Lett.* **2003**, *3*, 1481−1484.
(26) Morell, G.; Canales, E.; Weiner, B. In Situ Measurements of Methane and Acetylene Concentrations in a CVD Reactor by Infrared Spectroscopy. *Diamond Relat. Mater.* **1999**, *8*, 166−170.
(27) Morell, G.; González-Berríos, A.; Weiner, B. R.; Gupta, S. Synthesis, Structure, and Field Emission Properties of Sulfur-Doped Nanocrystalline Diamond. *J. Mater. Sci.: Mater. Electron.* **2006**, *17*, 443−451.
(28) Palomino, J.; Varshney, D.; Resto, O.; Weiner, B. R.; Morell, G. Ultrananocrystalline Diamond-Decorated Silicon Nanowire Field Emitters. *ACS Appl. Mater. Interfaces* **2014**, *6*, 13815−13822.
(29) Shakerzadeh, M.; Teo, E. H. T.; Sorkin, A.; Bosman, M.; Tay, B. K.; Su, H. Plasma Density Induced Formation of Nanocrystals in Physical Vapor Deposited Carbon Films. *Carbon* **2011**, *49*, 1733−1744.
(30) Xie, W.; Möbus, G.; Zhang, S. Carbon Nanotube to SiC Nanorod Conversion in Molten Salt Studied by EELS and Aberration Corrected HRTEM. *J. Phys. Conf. Ser.* **2010**, *241*, 012093−1−012093−4.
(31) Batson, P. E. Current Trends for EELS Studies in Physics. *Microsc., Microanal., Microstruct.* **1991**, *2*, 395−402.
(32) Shanov, V.; Yun, Y.; Schulz, M. Synthesis and Characterization of Carbon Nanotube Materials. *J. Univ. Chem. Technol. Metall.* **2006**, *41*, 377−390.
(33) Rinzler, A. G.; Liu, J.; Dai, H.; Nikolaev, P.; Huffman, C. B.; Rodríguez-Macías, F. J.; Boul, P. J.; Lu, A. H.; Heymann, D.; Colbert, D. T.; et al. Large-Scale Purification of Single-Wall Carbon Nanotubes: Process, Product, and Characterization. *Appl. Phys. A: Mater. Sci. Process.* **1998**, *67*, 29−37.
(34) Varshney, D.; Sumant, A. V.; Resto, O.; Mendoza, F.; Quintero, K. P.; Ahmadi, M.; Weiner, B. R.; Morell, G. Single-Step Route to Hierarchical Flower-like Carbon Nanotube Clusters Decorated with Ultrananocrystalline Diamond. *Carbon* **2013**, *63*, 253−262.
(35) Morell, G.; Vargas, I.; Manso, J.; Guzmán, J.; Weiner, B. In Situ Phase-Modulated Ellipsometry Study of the Surface Damaging Process of Silicon under Atomic Hydrogen. *Solid State Commun.* **2000**, *116*, 217−220.
(36) Kumar, M.; Ando, Y. Chemical Vapor Deposition of Carbon Nanotubes: A Review on Growth Mechanism and Mass Production. *J. Nanosci. Nanotechnol.* **2010**, *10*, 3739−3758.
(37) Che, G.; Lakshmi, B. B.; Martin, C. R.; Fisher, E. R.; Ruoff, R. S. Chemical Vapor Deposition Based Synthesis of Carbon Nanotubes and Nanofibers Using a Template Method. *Chem. Mater.* **1998**, *10*, 260−267.

DOI: 10.1021/acs.jpcc.5b01178
J. Phys. Chem. C 2015, 119, 21125−21134

(38) Teo, K.; Singh, C.; Chhowalla, M.; Milne, W. Catalytic Synthesis of Carbon Nanotubes and Nanofibers. *Encycl. Nanosci. Nanotechnol.* **2003**, *X*, 1−22.
(39) Yang, Z. H.; Zhou, Y. H.; Sang, S. B.; Feng, Y.; Wu, H. Q. Lithium Insertion into Multi-Walled Raw Carbon Nanotubes Pre-Doped with Lithium. *Mater. Chem. Phys.* **2005**, *89*, 295−299.
(40) Chen, H.; Xiao, Y.; Wang, L.; Yang, Y. Silicon Nanowires Coated with Copper Layer as Anode Materials for Lithium-Ion Batteries. *J. Power Sources* **2011**, *196*, 6657−6662.
(41) Kang, K.; Lee, H.-S.; Han, D.-W.; Kim, G.-S.; Lee, D.; Lee, G.; Kang, Y.-M.; Jo, M.-H. Maximum Li Storage in Si Nanowires for the High Capacity Three-Dimensional Li-Ion Battery. *Appl. Phys. Lett.* **2010**, *96*, 053110−1−053110−3.
(42) Green, M.; Fielder, E.; Scrosati, B.; Wachtler, M.; Moreno, J. S. Structured Silicon Anodes for Lithium Battery Applications. *Electrochem. Solid-State Lett.* **2003**, *6*, A75−A79.
(43) Lin, K.; Xu, Y.; He, G.; Wang, X. The Kinetic and Thermodynamic Analysis of Li Ion in Multi-Walled Carbon Nanotubes. *Mater. Chem. Phys.* **2006**, *99*, 190−196.
(44) Guo, Z.; Zhao, Z.; Liu, H.; Dou, S. Electrochemical Lithiation and de-Lithiation of MWNT−Sn/SnNi Nanocomposites. *Carbon* **2005**, *43*, 1392−1399.
(45) Yoshio, M.; Tsumura, T.; Dimov, N. Electrochemical Behaviors of Silicon Based Anode Material. *J. Power Sources* **2005**, *146*, 10−14.
(46) Zuo, P.; Yin, G.; Hao, X.; Yang, Z.; Ma, Y.; Gao, Z. Synthesis and Electrochemical Performance of Si/Cu and Si/Cu/graphite Composite Anode. *Mater. Chem. Phys.* **2007**, *104*, 444−447.
(47) Yang, S.; Song, H.; Chen, X. Electrochemical Performance of Expanded Mesocarbon Microbeads as Anode Material for Lithium-Ion Batteries. *Electrochem. Commun.* **2006**, *8*, 137−142.
(48) Li, J.; Dudney, N. J.; Nanda, J.; Liang, C. Artificial Solid Electrolyte Interphase to Address the Electrochemical Degradation of Silicon Electrodes. *ACS Appl. Mater. Interfaces* **2014**, *6*, 10083−10088.
(49) Cheng, Y.-W.; Lin, C.-K.; Chu, Y.-C.; Abouimrane, A.; Chen, Z.; Ren, Y.; Liu, C.-P.; Tzeng, Y.; Auciello, O. Electrically Conductive Ultrananocrystalline Diamond-Coated Natural Graphite-Copper Anode for New Long Life Lithium-Ion Battery. *Adv. Mater.* **2014**, *26*, 3724−3729.
(50) Liu, N.; Hu, L.; McDowell, M. T.; Jackson, A.; Cui, Y. Prelithiated Silicon Nanowires as an Anode for Lithium Ion Batteries. *ACS Nano* **2011**, *5*, 6487−6493.
(51) David, L.; Asok, D.; Singh, G. Synthesis and Extreme Rate Capability of Si−Al−C−N Functionalized Carbon Nanotube Spray-on Coatings as Li-Ion Battery Electrode. *ACS Appl. Mater. Interfaces* **2014**, *6*, 16056−16064.
(52) Bhandavat, R.; Singh, G. Stable and Efficient Li-Ion Battery Anodes Prepared from Polymer-Derived Silicon Oxycarbide-Carbon Nanotube Shell/core Composites. *J. Phys. Chem. C* **2013**, *117*, 11899−11905.
(53) Bhandavat, R.; Singh, G. Improved Electrochemical Capacity of Precursor-Derived Si(B)CN-Carbon Nanotube Composite as Li-Ion Battery Anode. *ACS Appl. Mater. Interfaces* **2012**, *4*, 5092−5097.
(54) Hu, L.; Wu, H.; Gao, Y.; Cao, A.; Li, H.; McDough, J.; Xie, X.; Zhou, M.; Cui, Y. Silicon-Carbon Nanotube Coaxial Sponge as Li-Ion Anodes with High Areal Capacity. *Adv. Energy Mater.* **2011**, *1*, 523−527.
(55) Dresselhaus, M. S.; Dresselhaus, G.; Saito, R.; Jorio, A. Raman Spectroscopy of Carbon Nanotubes. *Phys. Rep.* **2005**, *409*, 47−99.
(56) Lehman, J. H.; Terrones, M.; Mansfield, E.; Hurst, K. E.; Meunier, V. Evaluating the Characteristics of Multiwall Carbon Nanotubes. *Carbon* **2011**, *49*, 2581−2602.
(57) DiLeo, R. A.; Landi, B. J.; Raffaelle, R. P. Purity Assessment of Multiwalled Carbon Nanotubes by Raman Spectroscopy. *J. Appl. Phys.* **2007**, *101*, 0643071−0643075.
(58) Maurin, G. Electrochemical Lithium Intercalation into Multiwall Carbon Nanotubes: A Micro-Raman Study. *Solid State Ionics* **2000**, *136−137*, 1295−1299.
(59) Sohrabi, F.; Nikniazi, A.; Movla, H. Optimization of Third Generation Nanostructured Silicon-Based Solar Cells. *Sol. Cells - Res. Appl. Perspect. - InTech* **2013**, *1*, 1−26.
(60) Morell, G.; Katiyar, R. S.; Weisz, S. Z.; Balberg, I. Characterization of the Silicon Network Disorder in Hydrogenated Amorphous Silicon Carbide Alloys with Low Carbon Concentrations. *J. Non-Cryst. Solids* **1996**, *194*, 78−84.
(61) Meier, C.; Lüttjohann, S.; Kravets, V. G.; Nienhaus, H.; Lorke, A.; Wiggers, H. Raman Properties of Silicon Nanoparticles. *Phys. E* **2006**, *32*, 155−158.
(62) Liu, X. H.; Huang, J. Y. In Situ TEM Electrochemistry of Anode Materials in Lithium Ion Batteries. *Energy Environ. Sci.* **2011**, *4*, 3844−3860.
(63) Watanabe, H.; Hosoi, T. Fundamental Aspects of Silicon Carbide Oxidation. *Physics and Technology of Silicon Carbide Devices*; InTech: Rijeka, Croatia, 2013; Chapter 9, pp 235−250.
(64) Bashouti, M.; Pietsch, M.; Sardashti, K.; Brönstrup, G.; Schmitt, S. W.; Srivastava, S. K.; Ristein, J.; Arbiol, J.; Haick, H.; Christiansen, S. Hybrid Silicon Nanowires: From Basic Research to Applied Nanotechnology. *Nanowires - Recent Adv. - InTech* **2012**, *9*, 178−210.
(65) Ghita, R. V.; Logofatu, C.; Negrila, C. C.; Ungureanu, F.; Cotirlan, C.; Lazarescu, M.-F. Study of SiO2/Si Interface by Surface Techniques. *Crystalline Silicon—Properties and Uses*; Basu, S., Ed.; InTech: Rijeka, Croatia, 2011; Chapter 1, pp 23−42.
(66) Maruyama, T.; Naritsuka, S. Initial Growth Process of Carbon Nanotubes in Surface Decomposition of SiC. *Carbon Nanotub. - Synth. Charact. Appl. - InTech* **2011**, *2*, 29−46.
(67) Okpalugo, T. I. T.; Papakonstantinou, P.; Murphy, H.; McLaughlin, J.; Brown, N. M. D. High Resolution XPS Characterization of Chemical Functionalised MWCNTs and SWCNTs. *Carbon* **2005**, *43*, 153−161.
(68) Wepasnick, K. a; Smith, B. a; Bitter, J. L.; Howard Fairbrother, D. Chemical and Structural Characterization of Carbon Nanotube Surfaces. *Anal. Bioanal. Chem.* **2010**, *396*, 1003−1014.
(69) Hawaldar, R.; Merino, P.; Correia, M. R.; Bdikin, I.; Grácio, J.; Méndez, J.; Martín-Gago, J. a; Singh, M. K. Large-Area High-Throughput Synthesis of Monolayer Graphene Sheet by Hot Filament Thermal Chemical Vapor Deposition. *Sci. Rep.* **2012**, *2*, 682−1−682−9.
(70) Li, M.; Boggs, M.; Beebe, T. P.; Huang, C. P. Oxidation of Single-Walled Carbon Nanotubes in Dilute Aqueous Solutions by Ozone as Affected by Ultrasound. *Carbon* **2008**, *46*, 466−475.
(71) Radvanyi, E.; De Vito, E.; Porcher, W.; Jouanneau Si Larbi, S. An XPS/AES Comparative Study of the Surface Behaviour of Nano-Silicon Anodes for Li-Ion Batteries. *J. Anal. At. Spectrom.* **2014**, *29*, 1120−1131.
(72) Ensling, D.; Stjerndahl, M.; Nytén, A.; Gustafsson, T.; Thomas, J. O. A Comparative XPS Surface Study of Li2FeSiO4/C Cycled with LiTFSI- and LiPF6-Based Electrolytes. *J. Mater. Chem.* **2009**, *19*, 82−88.

DOI: 10.1021/acs.jpcc.5b01178
J. Phys. Chem. C 2015, 119, 21125−21134